ACS OMEGA

http://pubs.acs.org/journal/acsodf
Article

Synthesis of the NiO-Faujasite Nanocatalyst for Dry Reforming of Methane: The Effect of the Aniline Additive

Ari Susandy Sanjaya, Yahia Hakmi, Mohammed A. Sanhoob, Galal Nasser, Ali Rinaldi,* Oki Muraza, Assem T. Mohamed, Abdelbaki Benamor,* Mazen Khaled, Kifah S. M. Salih, Rashid Al-Hajri, and Arief C. Wibowo*

Cite This: *ACS Omega* 2025, 10, 16102−16113

Read Online

ACCESS | Metrics & More | Article Recommendations | Supporting Information

ABSTRACT: Dry reforming of methane (DRM) using a heterogeneous catalyst presents one of the CO_2 mitigation pathways to address global warming and climate change challenges. Such a suitable DRM catalyst with optimum activity and stability is still under intense research. We herein present a facile, slightly modified version of the conventional wet impregnation method to synthesize a NiO-faujasite nanocatalyst for DRM with the help of aniline, judiciously chosen based on the hard−soft acid−base (HSAB) principle. The resulting catalyst was characterized by the N_2 adsorption isotherm, PXRD, SEM/TEM, XPS, ^{29}Si solid-state NMR, H_2-TPR, NH_3-TPD, and DRM reaction, and its results were compared with those without aniline assistance. A smaller NiO nanoparticle with better dispersion was observed for our aniline-assisted sample resulting in a significant increase in activity (peaking at 86% CH_4 conversion with a H_2/CO ratio of 0.93) and stability for a 12 h time on stream. We hope that this work would pave the way to utilize the HSAB principle to synthesize more nanocatalysts with optimum overall performance.

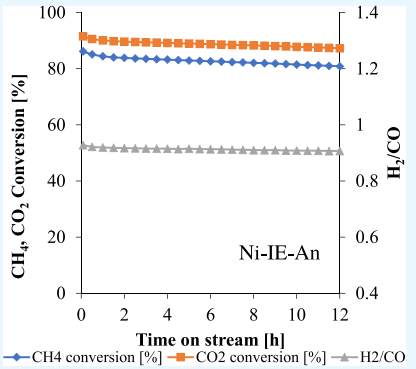

INTRODUCTION

Global warming and climate change occur due to the high concentration of anthropogenic CO_2 in the atmosphere because of our heavy dependence on fossil fuels.[1] An alarming increase of 50% in CO_2 concentration compared to the preindustrial era catalyzes global efforts for CO_2 abatements[2−6] from which many carbon capture, storage, and utilization (CCSU)-based research groups and institutions were established. An example of CO_2 utilization is CO_2 reduction, forming value-added chemicals such as formic acid, methane, methanol, and many more.[7−11] CO, another CO_2 reduction product, is an important C1-building block for Fischer−Tropsch and Monsanto/Cativa reactions and can be effectively produced via a reverse water gas shift (RWGS) reaction using a stable heterogeneous catalyst.[12,13] Another example of CO_2 mitigation is to reuse CO_2 combined with methane, the so-called dry reforming of methane (DRM), to form CO and H_2 (syngas) as raw materials to produce petrochemicals. Besides Rh and Ir, Ni nanoparticles are reported to be the most active elements for DRM with a high C−H activation ability and the latter is highly preferred due to its significantly lower cost.[14,15] There are, however, two major drawbacks currently found in using Ni nanoparticles as a catalyst, e.g., susceptible to sintering and coke formation, which unfortunately inactivate its catalytic activity. At highly endothermic DRM temperatures (over 600 °C), Ni nanoparticles incline to sintering due to possessing a low Tammann temperature of 581 °C.[15,16] Having multiple Ni active sites in close proximity, further, made Ni nanoparticles display favorable C−H cleavage and C−C coupling, which boost coke formation.[15,17−19] Increasing the O/C ratio to suppress coking by using a nonstoichiometric feedstock ratio (increasing the CO_2 mol ratio) could be an alternative pathway for a better DRM activity and stability.[20,21] Additional issues to consider are the activations of CH_4 and CO as they were reported as rate-limiting steps in DRM.[22] In terms of optimum nanoparticle size, it was reported that Ni with particle sizes of 2−3 nm display the best DRM activities, while the unwanted carbon whisker yield increases with increasing Ni particle size.[22] Therefore, like other catalytic processes, DRM still appeals for a stable heterogeneous catalyst with optimum performance.[15,23−33]

Metal-in-zeolite, typically synthesized by the impregnation method, is an example of a heterogeneous catalyst. A variety of metal cations have been successfully embedded using this method, ranging from noble, rare earth, and transition metals, giving excellent catalytic performances.[34] Despite being favored by industry due to its simple and cost-effective method, impregnation suffers from metal sintering, which results in a larger metal size, hence reducing catalytic performance. The

Received: October 20, 2024
Revised: March 9, 2025
Accepted: March 11, 2025
Published: April 18, 2025

lack of control in the location of inserted metal is another drawback reported for this method.[34]

One eye-catching, relatively new technique is the in situ, ligand-assisted zeolite synthesis wherein atomically dispersed metal catalysts (ADMC) and atomically precise metal clusters (APMC) are successfully synthesized.[35] Despite an enticing breakthrough in catalytic performance, this method, however, did not use the readily made or commercially available zeolites that chemical industries preferred to use. Inspired by the need to find an effective postsynthetic modification of commercial zeolite to form a stable heterogeneous catalyst, herein, we introduce a simple, aniline-assisted synthetic method to successfully disperse ∼5 nm NiO-sized clusters embedded within faujasite, showcasing higher yield and stability in the DRM reaction compared to those samples prepared without aniline. Based on the hard−soft acid−base (HSAB) principle, aniline, being a borderline base, should interact better with borderline acid, Ni^{2+}[36,37] therefore was chosen as the ligand to predisperse the Ni^{2+} precursor within faujasite pores. Pre- and post-DRM reaction results of these samples are compared and discussed in terms of textural properties, PXRD, electron microscopy images (SEM and TEM), XPS, ^{29}Si solid-state NMR, H_2-TPR, and NH_3-TPD, highlighting the advantage of aniline assistance during the postmodification process to obtain better NiO dispersion with smaller size and stronger NiO−support interactions, therefore better DRM catalytic performance.

EXPERIMENTAL SECTION

Postmodification Procedures. The following chemicals, zeolite Y or faujasite, H-FAU (Alfa Aesar, hydrogen form, SiO_2/Al_2O_3 = 80), aniline (Sigma-Aldrich), and nickel(II) nitrate (Sigma-Aldrich), were used as received without any further purification. Commercially available faujasite was immersed in aqueous solution of nickel(II) nitrate with varied mass ratios of faujasite to the metal precursor as well as varied mole ratios of aniline to water. The best performing nanocatalyst, named Ni-IE-An, was made using the mass ratio of 1:1 for faujasite and nickel(II) nitrate, respectively, with 0.22 mol of aniline to 0.38 mol of H_2O, with a detailed methodology as follows. The required metal salt precursor and the required amount of aniline were dissolved in 7 mL of deionized water, giving a total volume of ∼26.4 mL solution of H_2O and aniline. A 4.0 g amount of faujasite was then added into the solution and mixed using a magnetic stirrer for 1 day. The filtered powder was dried overnight at room temperature, followed by calcination at 550 °C for 5 h. For comparison with the Ni-IE-An sample, we also synthesized the NiO-faujasite sample using a similar condition as mentioned above, but without aniline, designated as Ni-IE. Another NiO-faujasite sample having a comparable NiO actual content was also made using a typical wet impregnation method,[34] termed Ni-I, for further DRM property assessments. We further varied NiO contents (5, 10, and 20 wt %) using the aniline-assisted method, named Ni-IE-An-5, Ni-IE-An-10, and Ni-IE-An-20, to assess the effect of NiO contents in terms of DRM-related properties. These calcined samples were then ready for characterization and DRM-related evaluations.

Zeolite Characterization. The nitrogen adsorption−desorption isotherm was utilized to evaluate the BET surface area, external surface area, pore volume, micropore volume, and mesopore volume using an ASAP2020 Micromeritics analyzer. The strength of zeolitic acidity was determined using temperature-programmed desorption of ammonia molecules by performing NH_3-TPD analysis (BELCAT II, MicrotracBel). The measurement was performed by preheating the sample (50 mg) to 500 °C for 1 h under continuous flow of helium with a flow rate of 50 mL/min; then, the sample was cooled to 100 °C. Following 10% ammonia in helium fed to the reactor tube for 30 min with a flow rate of 30 mL/min, the sample was flushed with helium for 45 min to remove the excess ammonia, and the temperature was ramped again to 600 °C at a ramping rate of 10 °C min^{-1} and the thermal conductivity detector (TCD) signal was recorded simultaneously.

Temperature-programmed reduction (H_2-TPR) was also performed to determine the ability of the synthesized materials in consuming hydrogen. The measurement was performed by preheating the sample (50 mg) to 500 °C to remove moisture and impurities under an argon environment with a flow rate of 50 mL/min. The sample was then cooled to 50 °C, and a mixture of hydrogen (5 mL/min) and argon (45 mL/min) was fed to the reactor tube for the reduction process. The temperature was ramped again to 700 °C at a ramping rate of 10 °C min^{-1} and the TCD signal was recorded simultaneously.

Powder X-ray Diffraction. Ground mixtures of polycrystalline powders of the samples were used to collect powder X-ray diffraction patterns using a Rigaku Ultima IV powder diffractometer (Cu Kα radiation λ = 1.5418 Å) over the 2θ range of 5−50°, with a step size of 0.02° and a scan speed of 0.25°/ min. The measured patterns were compared with those in the ICDD database.

TEM, SEM, and ICP-OES. Transmission electron microscopy (TEM) images were taken on a JEOL GrandARM 300 keV, 10 mA instrument using annular dark-field (ADF) and annular bright-field (ABF) detectors. The samples were prepared by grinding a small amount of the specimen and dispersing it ultrasonically in absolute ethanol. Subsequently, drops of this suspension were applied on a Cu grid (200 mesh) with a lacey carbon film, and ethanol was evaporated at room temperature.

A Quattro ESEM 400 high-resolution field emission scanning electron microscope (SEM) operating between 5 and 15 kV for SE, BSE images, and energy-dispersive X-ray analysis (EDX) was used for taking SEM images of the samples. Quantitative NiO contents of the samples were determined using an analytikjena PlasmaQuant PQ 9000 inductively coupled plasma-optical emission spectrometer (ICP-OES). Prior to the measurements, the samples (50 mg) were dissolved in aqua regia (0.5 mL) and HF (2 mL; 40 wt %), neutralized by boric acid (1.2 g), and diluted using 0.42 M HNO_3.[38]

XPS and ^{29}Si Solid-State NMR. X-ray photoelectron spectroscopy (XPS) studies were performed using a multiprobe photoelectron spectroscopy (Scienta Omicron, Germany) equipped with a monochromatic Al Kα X-ray source (1486.6 eV) operated at 300 W. Samples were analyzed under ultrahigh vacuum ($P < 10^{-8}$ mbar), whereas survey scans and high-resolution scans were collected using pass energies of 50 and 20 eV, respectively. A low-energy electron gun was employed for charge neutralization during the measurement. Binding energies were calibrated with respect to the C 1s binding energy at 284.6 eV. CasaXPS software was employed for the calibration as well as to estimate the surface nickel content on the catalyst surface. ^{29}Si solid-state NMR studies were performed using a JEOL LAMBDA 500 spectrometer operating at 99.35 MHz using a broadband CPMAS probe.

https://doi.org/10.1021/acsomega.4c09539
ACS Omega 2025, 10, 16102−16113

^{29}Si CPMAS spectra were acquired under Hartmann−Hahn matching at applied radio frequency fields of 36 kHz, using contact times of 5 ms and relaxation delays of 4 s. Typically, 15,000−20,000 transients were collected for the ^{29}Si experiments. Neat tetraethylorthosilicate (−82.4 ppm) was used as the reference of ^{29}Si.

Catalytic Evaluation. The prepared catalysts were evaluated for dry reforming in a fixed bed reactor (PID Microactivity-Effi reactor). The sample (100 mg) was packed in a quartz tube that has an internal diameter of 10 mm and a length of 30 cm between two layers of quartz wool. The sample was reduced in situ and preheated to 750 °C under helium flow (45 mL/min) and hydrogen flow (5 mL/min) at atmospheric pressure for 30 min. After that, the hydrogen and helium gases were stopped, and then, a mixture of methane and carbon dioxide (50:50) was fed to the reactor tube with a flow rate of 80 mL/min. The products were analyzed by online gas chromatography (GC-2014, Shimadzu). The GC was equipped with one flammable ionization detector (FID, GasPro column, 30 m length and 0.32 mm diameter) and a thermal conductivity detector (TCD, configured with two packed columns including molecular sieve 13X and HN columns).

RESULTS AND DISCUSSION

Considering the cost efficiency and a wider playground to show an impactful improvement of DRM catalytic performances on the use of borderline base, i.e., aniline, we selected the 5 wt % NiO content (with an actual NiO loading of 4.50 wt % based on ICP-OES) as the baseline, named the Ni-I sample. Note that the details on postmodification optimization are described in the Supporting Information and Figure S1. Having only about 40% CH_4 conversion and around 30% CO_2 conversion, the Ni-I baseline has a vast space for further significant improvement in DRM performances, and indeed, the aniline-assisted method, with the Ni-IE-An sample with a comparable actual NiO loading, exhibited significant improvement in DRM performances as shown later.

After optimizing the aniline-to-water mol ratio (variable (b) in the Supporting Information), while fixing the faujasite-to-nickel(II) nitrate mass ratio (variable (a) in the Supporting Information), we found the use of 0.22 mol of aniline and 0.38 mol of water, while fixing a 5 wt % NiO loading, to be the optimized synthetic conditions, i.e., the Ni-IE-An sample, and it exhibited an actual NiO loading (3.60 wt % based on ICP-OES) comparable to that of Ni-I (4.50 wt % based on ICP-OES). Since both samples are made from slightly different conditions, we then synthesized Ni-IE using an exactly similar method with Ni-IE-An but without aniline addition, to underline the true effect of the aniline additive. To select which NiO content made with the aniline method exhibits optimum stability and activity, we further synthesized 5, 10, and 20 wt % NiO contents and found that indeed, the 5 wt % NiO loading, i.e., Ni-IE-An, displays the best overall DRM performances. The optimum results are therefore reported herein to signify the effect of the aniline-assisted method on the structure and morphology of NiO-faujasite and its resulting DRM properties complemented by temperature-programmed techniques, in terms of H_2-TPR and NH_3-TPD.

We present the characterization and reaction performance of a catalyst system designed based on the understanding of how the DRM catalyst deactivates, mainly by sintering and coking. This was achieved in this work by using faujasite micropore surfaces to strongly interact with NiO nanoparticles, presumably due to application of the HSAB principle during the post-treatment synthesis of faujasite using the Ni^{2+} precursor with aniline addition. Strong interaction between borderline acid, Ni^{2+}, and borderline base, aniline, prior to calcination, evidently led to smaller NiO nanoparticle size with excellent distribution inside the faujasite micropore. Physical and chemical characterization measurements performed herein showed better NiO dispersion and stronger NiO-faujasite interaction when aniline was used in the catalyst preparation step (Ni-IE-An) compared to the NiO-faujasite catalysts prepared without aniline (Ni-I and Ni-IE). The improved DRM reaction activity and stability are attributed to better dispersion of NiO with smaller particle size (∼5 nm) and enhanced NiO-faujasite interaction that mitigates sintering and coking. Our result agrees with the literature consensus that small metallic NiO nanoparticles show significant resistance to carbon deposition.[22,39,40] Our work provides a simple, room temperature protocol using aniline in aqueous nickel(II) nitrate solution to generate a stable, highly dispersed NiO nanocatalyst on faujasite to significantly reduce deactivation during the DRM reaction.

Textural Properties of Calcined Samples. We measured the changes in the faujasite surface area and porosity after NiO impregnation using N_2 adsorption−desorption isotherms. Figure 1 shows the adsorption−desorption isotherms of the

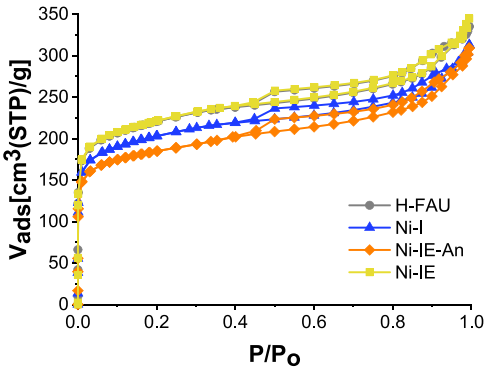

Figure 1. N_2 isotherms of faujasite (H-FAU) and calcined Ni-O-faujasite samples prepared with different techniques.

calcined samples. Table 1 presents the summary of the isotherm's analysis. The faujasite samples with NiO show similar isotherms to those of the pristine faujasite (H-FAU). All samples exhibit a type I adsorption isotherm with type H4 hysteresis loops. The type I isotherms are indicative of the microporous structure and the hysteresis indicates narrow, slit-shaped pores formed due to particle agglomeration.[41] The high C values from the BET equation are typical of strong interaction between N_2 and micropore walls in faujasite. The high external surface area in these samples suggests small particle size of the faujasite samples.

To highlight the micropore region, Figure S2 displays the adsorption isotherms as a semilog plot. All samples show similar adsorption capacity at low relative pressures, indicating similar micropore filling. The isotherms show no indication of micropore blocking after NiO addition. The sample with the lowest NiO loading, e.g., Ni-IE with 0.46 wt %, exhibits similar adsorption, BET area, micropore area, and external area values with those of the pristine faujasite support. However, for samples with higher NiO loadings, e.g., Ni-I (4.50 wt %) and

https://doi.org/10.1021/acsomega.4c09539
ACS Omega 2025, 10, 16102−16113

Table 1. Surface Area, Pore Analysis, and NiO Loading of Calcined NiO-Faujasite Samples Compared to Pristine Faujasite

sample	description	S_{BET}[a] (m^2/g)	C value	S_{micro}[b] (m^2/g)	S_{ext}[c] (m^2/g)	V_{micro}[c] (cm^3/g)	Ni wt %[d]
H-FAU	faujasite support	817	1832	527	290	0.14	NA
Ni-I	wet impregnation	752	1788	476	276	0.193	4.50
Ni-IE	without aniline	822	1807	523	299	0.211	0.46[e]
Ni-IE-An	with aniline	691	2018	472	220	0.190	3.60

[a]Roquerol requirement. [b]$S_{micro} = S_{BET} - S_{ext}$. [c]*t*-Plot method. [d]From ICP-OES measurements. [e]Due to its low Ni loading, the value was obtained from calibrated TPR measurements.

Ni-IE-An (3.60 wt %), the micropore filling starts to exhibit lower adsorption at a relative pressure of 5×10^{-4} as compared to that of the faujasite support. Although the Ni-IE-An sample has 20% less NiO content than the Ni-I sample, the former exhibits smaller adsorption amounts and smaller BET area. This finding suggests a greater influence of NiO inclusion on the microporosity of the faujasite in the Ni-IE-An sample than in the Ni-I sample. We further note that after Ni inclusions, the micropore volumes of all samples (Ni-I, Ni-IE, and Ni-IE-An) enhance as compared to that of the faujasite support, H-FAU. An increase in the micropore volume suggests an increase in adsorption sites upon Ni loading, which implies an increase in acidic sites, supported by NH_3-TPD and XPS results discussed in later sections. Such an increase can be ascribed to the introduction of more Lewis acid sites on the support due to the Ni^{2+} inclusion as nickel cations can act as electron acceptors.[42,43]

To demonstrate the effect of the NiO loading on the textural properties of faujasite, we prepared NiO-faujasite samples using the wet impregnation method (Ni-I) with various Ni^{2+} loadings (5, 10, 15, and 20 wt %) and measured their N_2 isotherms, Table S1. The isotherm analysis of the calcined samples demonstrates a monotonic decrease in adsorption, BET area, micropore area, and external area values with an increasing NiO content. This relation is due to the nonporous nature of the NiO particles impregnated in the faujasite support. Although BET and micropore area values cannot be taken as the true surface area of the samples, the trends indicate that all three samples preserve the zeolite micropore structures. Subsequent analysis will look at the crystal structure of the faujasite support and the characteristics of the NiO inclusions.

PXRD Results of Calcined Samples. We performed powder X-ray diffraction (PXRD) measurements to monitor the faujasite's integrity after NiO impregnation and calcination. The diffraction patterns in Figure 2 show that the diffraction peaks from the faujasite support are present in all samples. The relative intensities of the faujasite diffraction peaks remain similar in NiO-containing samples compared to those of the pristine faujasite. This shows that the structural integrity of the faujasite is preserved after the NiO impregnation and calcination steps.

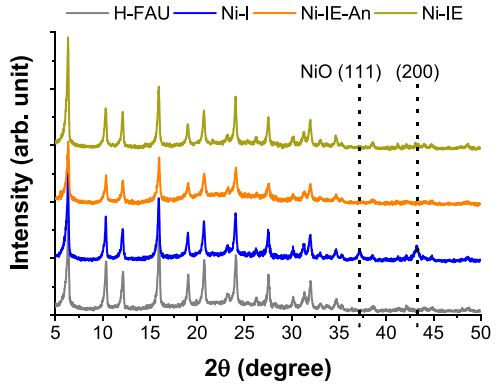

Figure 2. Powder XRD patterns of the faujasite support (H-FAU) and NiO-faujasite catalysts, Ni-I, Ni-IE, and Ni-IE-An.

Diffraction peaks for NiO (111) and (200) reflections at 37.2 and 43.2°, respectively, are observed for Ni-I and Ni-IE samples. The presence of NiO in the samples is expected, as the samples were calcined in air prior to characterization. These two peaks were absent from the bare faujasite (H-FAU) and our aniline-assisted NiO-faujasite sample (Ni-IE-An). Elemental analysis, using ICP-OES data in Table 1, shows that Ni-I and Ni-IE-An have comparable NiO loadings at 4.50 and 3.60 wt %, respectively. This result shows that the NiO particle sizes embedded in Ni-I and Ni-IE samples are large enough to be detected by X-ray diffraction, whereas finer sizes of NiO with an average particle size of ∼5 nm observed in the aniline-assisted method, the Ni-IE-An sample, could not be distinctively discerned by X-ray diffraction, which is probably due to extensive peak broadening typically observed at such a nanoparticle size range and the fact that the diffraction peaks are further obscured by the noise.[44] The presence of Ni species in Ni-IE-An was confirmed using ICP-OES, TEM, XPS, and ^{29}Si solid-state NMR and will be described in later sections.

Electron Microscopy of Calcined Samples. We analyzed the samples' morphology using high-resolution SEM as presented in Figure 3. In general, samples after NiO inclusion and calcination exhibit a morphology similar to that of the faujasite support. The particle size ranges from 0.3 to 1.0 μm, and they form agglomerates. SEM images in Figure 3a,c (with additional images of Ni-IE shown in Figure S3) show dispersed NiO nanoparticles on the faujasite particles with average diameters of 80 and 29 nm for Ni-I and Ni-IE samples, respectively. Such dimensions of nanoparticles, however, were undetected in the Ni-IE-An sample (Figure 3e). The corresponding BSE images acquired for each sample demonstrate brighter contrast for the NiO nanoparticles than the faujasite support particles, as observed in Ni-I and Ni-IE samples (Figure 3b,d). The brighter contrast indicates that the nanoparticles are composed of heavier elements than the silicon and oxygen of the faujasite support, i.e., evidence for Ni species embedded on the faujasite support. As the samples were calcined in air, Ni particles must be in an oxidized state (NiO). This corroborates the PXRD data in Figure 2 that shows NiO diffractions in Ni-I and Ni-IE samples. Furthermore, elemental mapping analysis with EDX (Figure S4) verifies that the bright nanoparticles are composed of nickel.

In comparison, SE and BSE images for Ni-IE-An in Figure 3e,f (with additional images shown in Figure S5) show that NiO nanoparticles are undetected. Nevertheless, ICP-OES measurement confirms the presence of nickel in Ni-IE-An

https://doi.org/10.1021/acsomega.4c09539
ACS Omega 2025, 10, 16102−16113

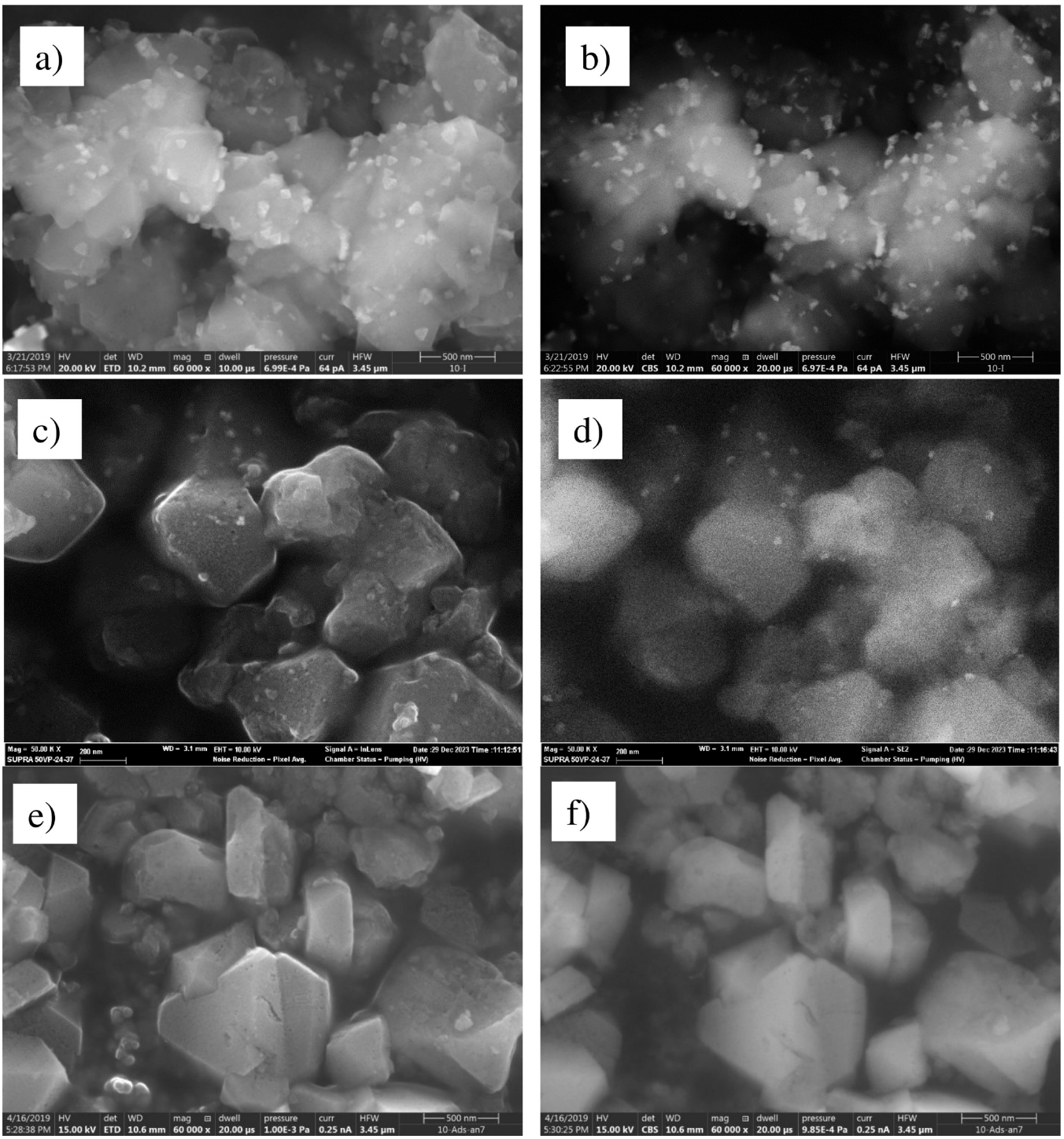

Figure 3. SEM images of the calcined samples acquired using SE signals and the corresponding BSE signals for Ni-I (a, b), Ni-IE (c, d), and Ni-IE-An (e, f).

(Table 1), suggesting that the Ni species embedded in Ni-IE-An are too small for SEM to resolve. Hence, the Ni-IE-An sample was further characterized with HR-TEM to determine nickel species' size and their distribution on the faujasite support. Figure 4 presents the bright-field TEM and corresponding high-angle annular dark-field (HAADF) images for the Ni-IE-An sample. The HAADF image reveals finely dispersed NiO nanoparticles on the faujasite support with average sizes ∼5 nm, and hence, they were undetected by SEM. There is no nanoparticle in this size range observed in the Ni-I and Ni-IE samples. Hence, electron microscopy analysis clearly demonstrates that the aniline method, Ni-IE-An, produces the best Ni species dispersion and the smallest nanoparticle size on the faujasite support compared to the other two methods (Ni-I and Ni-IE).

XPS and ^{29}Si Solid-State NMR of Calcined Samples. In order to correlate with our PXRD, SEM, and TEM results, especially in the case of the Ni-IE-An sample, we conducted XPS and ^{29}Si solid-state NMR, in particular to determine whether the as-calcined samples are oxidic or elemental Ni.

https://doi.org/10.1021/acsomega.4c09539
ACS Omega 2025, 10, 16102−16113

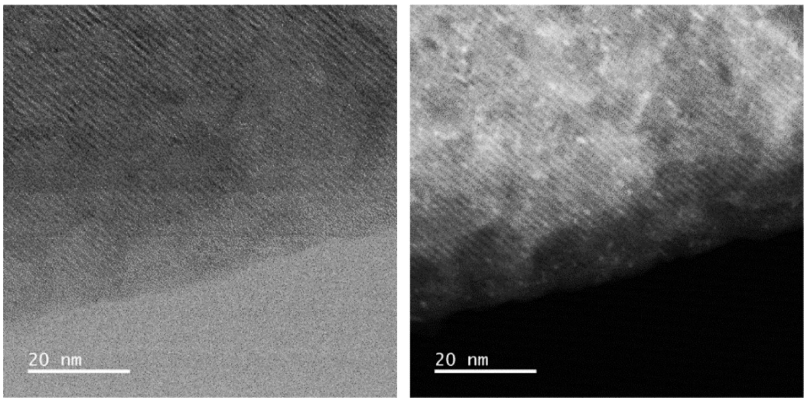

Figure 4. HR-TEM of the calcined Ni-IE-An sample showing the bright-field and corresponding HAADF images.

XPS analysis shows that all calcined samples, in general, exhibit the expected peak position range for Si 2p, C 1s, and O 1s in comparison to literature values for H-FAU.[45] Al 2p peak positions, however, display shifts to lower binding energies for Ni-I and Ni-IE samples as compared to that of H-FAU. Unlike the other two samples, the Al 2p peak of Ni-IE-An returned to higher binding energy (74.40 eV), Table S2, in a similar region to that of H-FAU (74.70 eV), which implies a higher oxidation state of Al compared to those of Ni-I and Ni-IE samples. Knowing the fact that Ni can be an electron acceptor,[42] electron transfer may occur from Al to Ni particularly for the Ni-IE-An sample, making the former to be in a higher oxidation state (3+), which corresponds to the 74.40 eV peak position for Al 2p of Ni-IE-An, while the Ni 2p peak in this sample exhibits 854.40 eV binding energy, consistent with the lower oxidation state (2+) of Ni, quite a distance from the Ni^{3+} binding energy of 855.50 eV.[46,47] Such electron transfer could lead to an increase in acidity after oxidic Ni inclusion, in line with an increase in the micropore volume as discussed in the textural property section as well as in NH_3-TPD observation as discussed later.

From the XPS survey, we also observed that all samples do not have metallic Ni due to the absence of a 852.4 eV peak, Figure 5.[15] There is no clear shift on Ni $2p_{3/2}$ and $2p_{1/2}$ peaks of all samples, which imply a similar oxidation state of Ni for all samples, Figure S6, and their comparatively smaller binding energy to other Ni-zeolite catalysts[15] suggests that our samples have a lower oxidation state of Ni.

The surface content Ni in Ni-IE-An was only 0.14 at. %, Figure 5, suggesting that majority of the Ni species are exclusively located within the faujasite framework, in agreement with our PXRD, SEM, and TEM results. Further, based on ^{29}Si solid-state NMR results, a larger disruption of the Si−O−Si network of faujasite is observed in the case of the Ni-IE-An sample, as its Si peak width is widened compared to other samples, Figure S7, indicating a stronger interference of paramagnetic Ni^{2+} onto the Si−O−Si network in this case, which implies a stronger interaction between NiO and the faujasite support. Ni surface contents for Ni-I and Ni-IE samples were 1.59 and 0.10 atomic %, respectively, implying that oxidic nickel species coexist on the surface and within the framework for Ni-I. Ni-IE, on the other hand, and its oxidic nickel species are mostly on the surface of the faujasite.

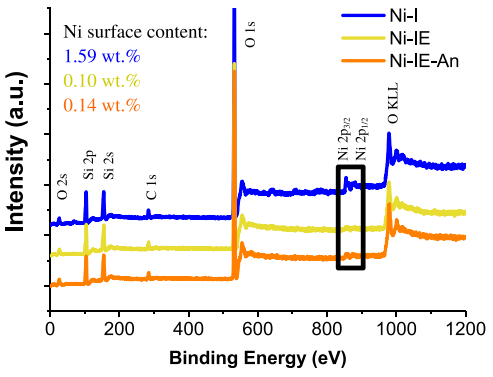

Figure 5. XPS full spectra of Ni-I, Ni-IE, and Ni-IE-An samples showing Ni surface contents.

H_2-TPR and NH_3-TPD of Calcined Samples. We characterized the reducibility of NiO inclusions in the calcined samples with the H_2-TPR method (Figure 6a). The measurements aim to gain insight into the size and chemical interaction of NiO with the faujasite support. The area under the curve is proportional to the NiO loading obtained from ICP-OES where Ni-I ≈ Ni-IE-An > Ni-IE. The TPR profiles for Ni-I and Ni-IE exhibit a similar pattern; an asymmetric broad peak with a maxima at 390 °C. Meanwhile, Ni-IE-An shows a broad curve composed of at least two peaks: one small peak centered at 390 °C and a larger peak centered at 540 °C. The broad reduction peaks in the Ni-IE-An sample indicate NiO species with varying sizes and/or degrees of the NiO−support interaction in the calcined state. Significant H_2 consumption above 650 °C is only observed for the Ni-IE-An sample. NiO species in the Ni-IE-An sample shows the highest resistance to reduction compared to those of Ni-I and Ni-IE samples. This may suggest a smaller NiO size, supporting our electron microscopy images, Figures 3 and 4. It may also imply a stronger interaction of NiO with the faujasite support in conjunction with our ^{29}Si solid-state NMR (Figure S7) result. Stronger NiO−support interaction, however, is better suited in explaining higher reduction temperature in the Ni-IE-An sample as nanoparticle size reduction does not guarantee higher reduction temperature.[48,49]

From the thermodynamics of NiO reduction, NiO nanoparticles exhibit a more positive standard free energy due to their high surface-to-volume ratio compared to bulk NiO. Similarly, the metal−support interactions of these finely dispersed NiO with faujasite will also make the standard free energy change more positive.[50] The lower reducibility of NiO species in this Ni-IE-An system can also be ascribed to NiO confinement in faujasite micropores and in terms of its acidity. NiO species confined in faujasite pores, i.e., <1 nm in size, and

https://doi.org/10.1021/acsomega.4c09539
ACS Omega 2025, 10, 16102−16113

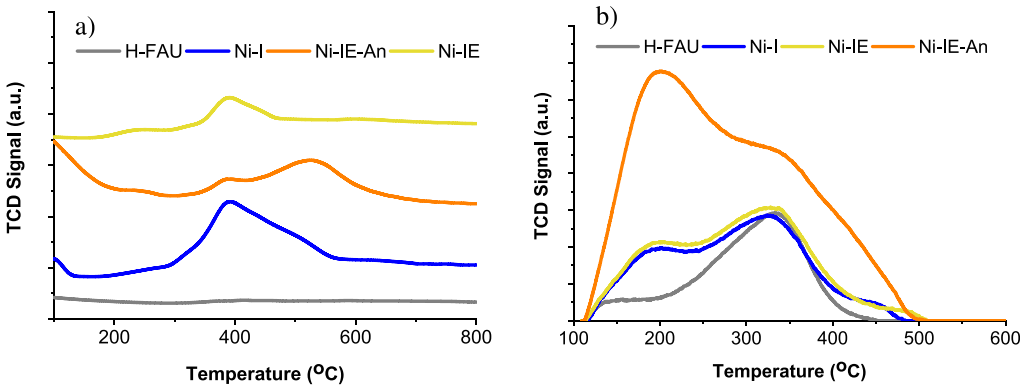

Figure 6. Temperature-programmed chemisorption analysis of calcined faujasite support (H-FAU) and NiO-faujasite catalysts: (a) H_2-TPR and (b) NH_3-TPD.

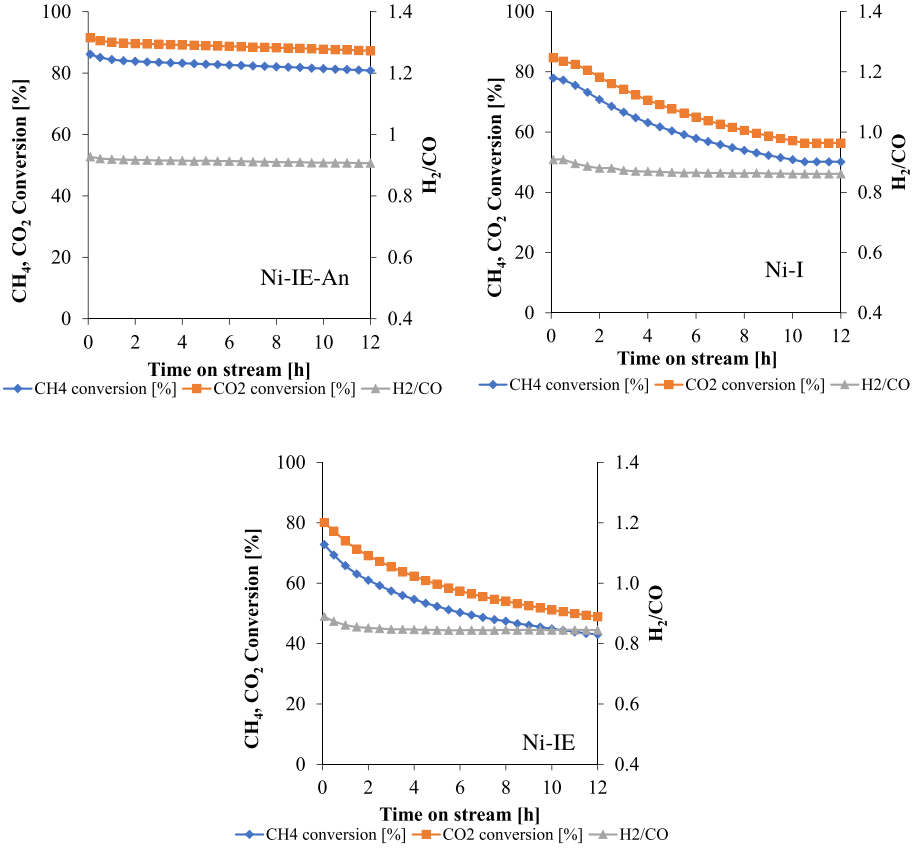

Figure 7. Reactivity test for DRM reactions of the catalysts showing CH_4 and CO_2 conversions and the H_2/CO ratio as a function of time on stream (TOS). Reaction conditions: 750 °C, GHSV = 48,000 mL h^{-1} g^{-1}, with a CH_4:CO_2 ratio of 1 at atmospheric pressure.

possible H_2O accumulation in the channel will also retard the reduction process. This can be understood from the second term in the thermodynamic expression of NiO reduction in the equation below, which shows how the free energy change depends on the P_{H_2O}/P_{H_2}.

$$\Delta G = \Delta G^{o} + RT \ln P_{H_2O}/P_{H_2}$$

$$NiO + H_2 \rightarrow Ni + H_2O$$

In the case of the Ni^{2+}-exchanged zeolite, the complex TPR profile can be explained by the following equation:

$$Ni^{2+}(\text{exchanged with zeolite}) + H_2 \rightarrow Ni^{0} + 2H^{+}$$

Here, the proton generated from the reduction of Ni^{2+} is captured by the lattice oxygen in the faujasite crystal to form hydroxyl groups. With this mechanism, the presence of the total Bronsted acidities in the faujasite support will make the reduction of Ni^{2+} less favorable, resulting in a higher TPR peak temperature as observed in our Ni-IE-An case.[51,52]

We also performed ammonia temperature-programmed desorption (NH_3-TPD) experiments to probe acid sites in the samples. The NH_3-TPD profiles of the calcined samples in Figure 6b display mainly two irregular desorption peaks. The first peak extends from 110 to 290 °C and centered around 190 °C. The second peak extends from 125 to 500 °C and centered around 310 °C. The first and second peaks indicate the existence of weak and strong acid sites, respectively. Figure

https://doi.org/10.1021/acsomega.4c09539
ACS Omega 2025, 10, 16102−16113

Table 2. Summary of DRM Performance, BET Surface Area, and NiO Size of the Calcined NiO-Faujasite Samples

sample	Ni content (wt %)	S_{BET} (m^2/g)	CH_4 conversion (%)	CO_2 conversion (%)	H_2/CO	NiO size (nm)
Ni-I	4.50	817	80−50	84−56	0.90−0.86	80
Ni-IE	0.46	822	73−43	80−49	0.89−0.84	29
Ni-IE-An	3.70	691	86−81	90−87	0.93−0.90	5.0

6b shows that NiO-containing samples have a higher total acidity than the parent zeolite support, especially for the weak acid sites. Ni-I and Ni-IE samples show a similar moderate increase of weak acid sites, whereas the increase is more pronounced for the Ni-IE-An sample.

The above-mentioned results highlight how aniline affects the faujasite's acid density after NiO inclusions. NH_3-TPD of calcined samples, Figure 6b, showed an increase in the density of weak acid sites for all NiO-faujasite samples. The increase is more pronounced for samples prepared with aniline, Ni-IE-An, supporting the XPS result on the possibility of electron transfers from Al to Ni after Ni inclusions. Such an increase in acidity is also aligned with micropore volume enhancement, as described earlier. It has been suggested that the increase in weak acid density in the NiO-zeolite system is due to hydrolysis of the Ni-exchanged zeolite as shown in the equation below.[53,54]

$$Ni^{2+}(\text{exchanged with zeolite}) + H_2O \rightarrow Ni(OH)^+ + H^+$$

An increase in the density of weak acid sites was previously reported for faujasite and other zeolite systems after NiO inclusion.[52,55] The NH_3-TPD data further illustrate how the change in acidity following one reducing step (of the calcined samples) depends on the dispersion of NiO in the faujasite support, Figures S8 and S9. For the samples prepared with aniline, Ni-IE-An, there was a significant decrease in acidity, especially for the weak acid density, after a reduction step. For the samples prepared without aniline, Ni-I, where larger NiO nanoparticles were observed, the change in acidity after one reduction step was insignificant. The intensity of the NH_3-TPD peak of Ni-IE-An at around 190 °C (weak acid density) is still higher than that of the faujasite support (H-FAU), Figure S9, which may suggest that after one reduction step, the Ni-IE-An sample has coexisting metallic and partially unreduced oxidic Ni. Such a mixed state was also reported in another Ni-zeolite catalyst system.[15]

A similar trend of decreasing acidity after reduction was reported for highly dispersed NiO in silica.[56] This supports the idea that the increase in weak acid density observed in the aniline-prepared samples is related to a high NiO dispersion in faujasite. We would further propose that the NH_3-TPD data herein indicate that aniline may promote formation of Ni^{2+}-exchanged faujasite, in agreement with earlier reports.[53,54] Further in-depth studies to prove Ni−O−Si exchange and mixed (metallic and oxidic Ni) state formation during the DRM process and investigations on aniline in controlling the weak acid density in the NiO-zeolite system are ongoing in our lab, especially for application in structure-sensitive reactions and the acid density of zeolitic catalysts.

Both temperature-programmed techniques performed in this work agree with electron microscopy, PXRD, XPS, and ^{29}Si solid-state NMR, pointing to the high dispersion of smaller NiO nanoparticles in faujasite with a stronger NiO-faujasite interaction, when prepared using aniline as an additive, i.e., the Ni-IE-An as-calcined sample.

DRM Performance of Calcined Samples. The NiO-faujasite samples were tested for their performance in dry reforming of methane (DRM) reaction under isothermal conditions at 750 °C, and the results are shown in Figure 7 and summarized in Table 2. The calcined samples were reduced in H_2 at 750 °C in the reactor prior to the DRM test.

All samples exhibit about 6% higher CO_2 conversion compared to CH_4 conversion for a 12 h time on stream (TOS). This may be due to the side reaction such as the reverse water gas shift (RWGS) reaction that consumes CO_2.[57] Ni-IE-An demonstrates the highest CO_2 and CH_4 conversions at a 12 h TOS. In the first hour, Ni-IE-An shows 86% CH_4 conversion and then slightly decreases to 81%, exhibiting stable and steady conversion at 81% up to a 12 h TOS. In contrast, both Ni-I and Ni-IE exhibit a significant loss in CH_4 conversion at a 12 h TOS. For Ni-I, CH_4 conversion decreases from 80 to 50%, while for Ni-IE, CH_4 conversion decreases from 73 to 43%. The superior activity and stability of Ni-IE-An can be attributed to a smaller NiO nanoparticle size with better dispersion (as suggested by electron microscopy and PXRD results and as implied by XPS, H_2-TPR, and NH_3-TPD studies) and stronger NiO-faujasite interactions (as indicated by ^{29}Si solid-state NMR and H_2-TPR analysis), respectively.

The H_2 selectivity decreases slightly for all samples for a 12 h TOS, Figure 7. The H_2/CO ratios for Ni-I and Ni-IE decrease from 0.90 to 0.86 and 0.89 to 0.84, respectively. Ni-IE-An demonstrates slightly better stability, with the H_2/CO ratio showing a lower drop from 0.93 to 0.90. This deviation from the ideal ratio of 1 is due to side reactions such as RWGS that consume H_2 and generate CO.[57] The H_2 selectivity trend here indicates that the selectivity is relatively insensitive to the NiO dispersion on the faujasite support. Ni-I and Ni-IE-An with very different NiO dispersions and with different CO_2 and CH_4 conversion stability still show comparable H_2/CO ratios, supporting the assumption above.

To further confirm that the 5 wt % NiO content, synthesized using the aniline-assisted method, is the best overall DRM-related performance, we investigated the NiO content (5, 10, and 20 wt %) effects on the resulting morphology (evaluated using PXRD and TEM), reducibility (H_2-TPR), acid sites (NH_3-TPD), and DRM activity and stability. Our results indicate that indeed, 5 wt % NiO displays the highest CO_2 and CH_4 conversions, showing a stable ∼90% for both conversions up to a 26 h TOS with a steady ∼0.98 H_2/CO ratio, Figure S10. A clear, monotonic decrease in CO_2 and CH_4 conversions as well as the H_2/CO ratio is observed for 10 and 20 wt % NiO loadings made with the aniline method, Figures S11 and S12, respectively. Further, a higher reducibility temperature was observed in H_2-TPR of 5 wt % NiO, compared to those of 10 and 20 wt % NiO, Figure S13. In comparison with those of other contents made by the aniline method, a higher weak acid density can be inferred from NH_3-TPD of 5 wt % NiO, Figure S14, which implies better NiO dispersion in conjunction with TEM results, Figures S15−S17. The above results are derived from smaller NiO size and better dispersion for high DRM activity as well as better NiO-faujasite interaction for DRM

https://doi.org/10.1021/acsomega.4c09539
ACS Omega 2025, 10, 16102−16113

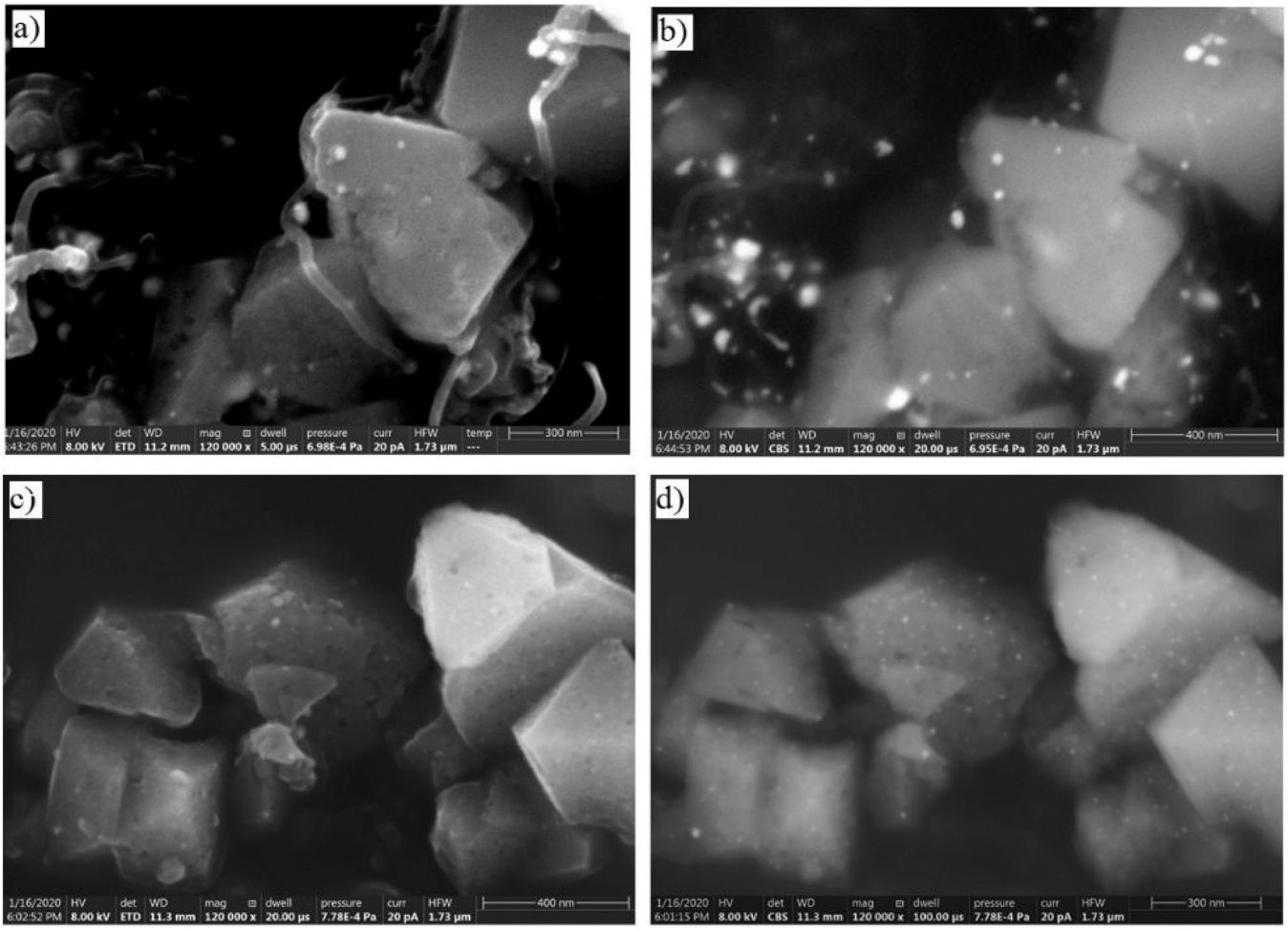

Figure 8. SEM analysis of catalyst samples after a 12 h TOS of DRM reactions. SE (a) and BSE images (b) for Ni-I and SE (c) and BSE (d) images for Ni-IE-An.

stability, observed in a 5 wt % NiO content. Based on TEM images, the average NiO particle sizes are 5, 11, and 13 nm for 5, 10, and 20 wt %, respectively, Figures S15, S16, and S17, respectively. The absences of NiO (111) and (200) reflections at 37.2 and 43.2°, respectively, are observed for all NiO contents' PXRD patterns made by the aniline method, Figure S18, further corroborating the advantage of aniline use in these cases. The results presented above stress that the 5 wt % NiO loading, i.e., the Ni-IE-An sample, is the optimum amount in terms of the NiO loading vs DRM performances.

Previous catalyst preparation studies using aqueous solution of the $Ni(NO_3)_2$ precursor have shown that solvated ion $Ni(H_2O)_6^{2+}$ is small enough to enter faujasite pores and other zeolite systems with smaller pores such as MOR, BETA, and CHA zeolites.[58−61] Without a strong interaction with zeolite micropore walls, the solvated Ni^{2+} species will migrate out to the external surfaces during drying and calcination. This will result in large NiO particles on the external zeolite surfaces. The weak interaction between Ni^{2+} and zeolite micropore walls has been attributed to the low polarizability of Ni^{2+} ion.[59,61]

Our data indicate that the presence of aniline in the precursor solution, while limiting the amount of aniline-modified Ni^{2+} precursors to go inside the faujasite micropores, suppresses Ni^{2+} migration, resulting in a smaller NiO size with a high level of dispersion and a stronger interaction with the faujasite micropore wall after calcination. Considering the harsh calcination conditions at 550 °C, during which water desorbs, nitrate decomposes, and aniline is removed, it is reasonable to assume that the role of aniline in promoting the interaction between Ni^{2+} and the faujasite micropore wall takes place during the soaking to drying stage and probably at the beginning of the calcination step. Our data showed that the interaction is strong enough to withstand the calcination, reduction, and to a large extent, the DRM reaction steps.

Aniline, with a molecular diameter of 0.67 nm, is small enough to enter faujasite pores.[62] Aniline adsorption on zeolite was shown not to be affected by the Si/Al ratio. Furthermore, it has been suggested that aniline is not ionized at moderate pH.[63] Therefore, we expect that a weak interaction would be observed between aniline and the strong Bronsted acid sites on faujasite micropores.

Further, the interaction between aniline, a borderline base, and Ni^{2+}, a borderline acid, can be understood from the HSAB theory. The HSAB theory describes that hard acids prefer to coordinate with hard bases and soft acids with soft bases. Similarly, borderline bases tend to interact with borderline acids.[36,37,64] The selectivity of borderline base moieties to borderline acid ions, such as Ni^{2+} in aqueous system, has been reported in the study of selective binding or exchange of metal ions in different compounds.[36,37,64,65] A similar strategy using organic additives in catalyst preparation to enhance metal ion complex interactions with zeolite micropores has been recently

https://doi.org/10.1021/acsomega.4c09539
ACS Omega 2025, 10, 16102−16113

reported.[61] The comprehensive and eloquent work demonstrated how the additive with amine and thiol groups facilitates the interaction between metal ions and small pore zeolites to encapsulate metal nanoparticles inside of zeolite micropores.

We speculate that the coordination between aniline and hydrated Ni^{2+} in aqueous solution weakens the Ni^{2+} coordination sphere, allowing better interaction with the bridging oxygen on faujasite micropore walls. The amine moiety of the aniline presumably formed dynamic acid−base interactions with faujasite's bridging oxygens to enhance metal−support interactions, even after calcination, henceforth higher catalyst stability,[61] as observed in our Ni-IE-An case. Whether the interaction between Ni^{2+} species and bridging oxygen charged species is electrostatic or grafting is not yet clear from our current data. Although the latter would have generated a stronger interaction, which could explain the sintering resistance during the high-temperature DRM test, spectroscopic studies are necessary to probe the interaction between Ni^{2+} and the faujasite micropore wall and will be reported in our subsequent investigation. Furthermore, experiments will be performed to look at the aniline's, and other bases, suitability to promote dispersion of NiO and other catalytically active oxides in other zeolite systems (with smaller pore size and varying Si/Al ratios), appraised using the HSAB principle.

Post-DRM Analysis on Spent Samples. We examined spent Ni-I, Ni-IE, and Ni-IE-An samples with high-resolution SEM to analyze the NiO particles after a 12 h TOS. Ni-I and Ni-IE-An represent samples with comparable NiO loadings that have different DRM activities. Figure 8 shows the SE and BSE images for the two spent samples (Ni-I and Ni-IE-An). Significant growth of carbon filaments was observed in the spent Ni-I sample. The *Z*-contrast BSE image confirms the encapsulation of NiO particles with a broad size distribution within the filaments. In contrast, carbon filaments were absent in the Ni-IE-An spent sample. Nevertheless, uniform bright nanoparticles were observed in the BSE image of the spent Ni-IE-An (Figure 8d). Such a feature was absent in the freshly calcined Ni-IE-An sample (Figure 3f).

The electron microscopy images in Figure 8 demonstrate that the Ni-I catalyst deactivates predominantly due to coking. The coking is driven by the existence of already large NiO particles prior to the reaction (Figure 3a,b). After the DRM reaction, the sintering of NiO nanoparticles in the Ni-I sample resulted in a larger NiO size, Figure 8a,b. A similar result was observed also for spent Ni-IE samples, Figure S19, with NiO sizes ranging from 20 to 90 nm for both spent samples. The slight decrease in CH_4 and CO_2 conversions, discussed earlier in the DRM performance section, may also be due to NiO sintering, with approximate NiO sizes between 10 and 15 nm (still comparatively smaller sizes than as-calcined Ni-I and Ni-IE samples), observed in the spent Ni-IE-An sample, Figure 8d. These results underline the crucial role of aniline assistance in making a stronger NiO-faujasite support interaction in the case of the Ni-IE-An sample.

CONCLUSIONS

We showcased the advantages of aniline assistance, appraised by the HSAB principle, in designing a NiO-faujasite catalyst for dry reforming of methane. Such a catalyst, Ni-IE-An, exhibited a smaller NiO nanoparticle size, ∼5 nm, and better dispersion embedded majority within the faujasite support that led to a notable DRM performance in terms of activity and stability for a 12 h TOS, compared to samples without aniline use, as proven from the observed textural, morphological, structural, temperature-programmed chemisorption, and DRM property evaluations. Post-DRM measurement also favored Ni-IE-An performance as there was no indication of carbon filament formation after a 12 h TOS, implying better metal−support interactions, in agreement with our H_2-TPR and ^{29}Si solid-state NMR studies, to significantly reduce catalyst deactivation, hence better stability.

ASSOCIATED CONTENT

Supporting Information

The Supporting Information is available free of charge at https://pubs.acs.org/doi/10.1021/acsomega.4c09539.

Further details in Tables S1-S2, and Figures S1−S19 (PDF)

AUTHOR INFORMATION

Corresponding Authors

Ali Rinaldi − *Department of Chemistry, TUM School of Natural Sciences, Technical University of Munich, Garching 85747, Germany*; Email: ali.rinaldi@tum.de

Abdelbaki Benamor − *Gas Processing Center, College of Engineering, Qatar University, Doha, Qatar*; orcid.org/0000-0003-0150-8431; Email: benamor.abdelbaki@qu.edu.qa

Arief C. Wibowo − *Department of Chemistry, College of Sciences, Sultan Qaboos University, Muscat PC 123, Oman*; orcid.org/0000-0002-2454-4307; Email: a.wibowo@squ.edu.om

Authors

Ari Susandy Sanjaya − *Department of Chemical Engineering, Mulawarman University, Samarinda, East Kalimantan 75119, Indonesia*

Yahia Hakmi − *Department of Chemistry, King Fahd University of Petroleum and Minerals, Dhahran 31261, Saudi Arabia*

Mohammed A. Sanhoob − *Interdisciplinary Research Center for Hydrogen and Energy Storage (IRC-HES), King Fahd University of Petroleum and Minerals, Dhahran 31261, Saudi Arabia*; orcid.org/0000-0002-0574-5058

Galal Nasser − *Interdisciplinary Research Center for Hydrogen and Energy Storage (IRC-HES), King Fahd University of Petroleum and Minerals, Dhahran 31261, Saudi Arabia*; orcid.org/0000-0001-7468-5944

Oki Muraza − *Research & Technology Innovation, PT. Pertamina (Persero), Jakarta 13920, Indonesia*

Assem T. Mohamed − *Gas Processing Center, College of Engineering, Qatar University, Doha, Qatar*

Mazen Khaled − *Department of Chemistry and Earth Sciences, Qatar University, Doha, Qatar*; orcid.org/0000-0002-8826-2413

Kifah S. M. Salih − *Department of Chemistry and Earth Sciences, Qatar University, Doha, Qatar*; orcid.org/0000-0002-0509-1875

Rashid Al-Hajri − *Department of Petroleum and Chemical Engineering, College of Engineering, Sultan Qaboos University, Muscat PC 123, Oman*

Complete contact information is available at: https://pubs.acs.org/10.1021/acsomega.4c09539

https://doi.org/10.1021/acsomega.4c09539
ACS Omega 2025, 10, 16102−16113

Author Contributions

The manuscript was written through contributions of all authors. All authors have given approval to the final version of the manuscript.

Notes

The authors declare no competing financial interest.

■ ACKNOWLEDGMENTS

The authors would like to acknowledge SQU-QU International Co-Funding Program no. CL/SQU\QU/SCI/24/02 and Qatar University internal grant no. IRCC 2024-003. The authors also thank the Interdisciplinary Research Center for Hydrogen and Energy Storage (IRC-HES) and the Department of Chemistry at King Fahd University of Petroleum and Minerals, Saudi Arabia, for hosting and supporting the research activities in its early stage. The authors further acknowledge Prof. Marc Willinger of Department of Chemistry, TUM, Germany, for TEM measurements and discussion; Dr. Myo Tay Zar Myint of Surface Science Lab, Department of Physics, Sultan Qaboos University, Oman, for XPS measurement and analysis; and Prof. Joao Rocha of Department of Chemistry, University of Aveiro, Portugal, for ^{29}Si solid-state NMR measurement and analysis.

■ REFERENCES

(1) Gulati, S.; Vijayan, S.; Mansi; Kumar, S.; Harikumar, B.; Trivedi, M.; Varma, R. S. Recent Advances in the Application of Metal-Organic Frameworks (MOFs)-Based Nanocatalysts for Direct Conversion of Carbon Dioxide (CO2) to Value-Added Chemicals. *Coord. Chem. Rev.* **2023**, *474*, No. 214853.

(2) Shi, D.; Heyte, S.; Capron, M.; Paul, S. Catalytic Processes for the Direct Synthesis of Dimethyl Carbonate from CO2 and Methanol: A Review. *Green Chem.* **2022**, *24* (3), 1067−1089.

(3) Qiao, J.; Liu, Y.; Hong, F.; Zhang, J. A Review of Catalysts for the Electroreduction of Carbon Dioxide to Produce Low-Carbon Fuels. *Chem. Soc. Rev.* **2014**, *43* (2), 631−675.

(4) Ramyashree, M. S.; Priya, S. S.; Freudenberg, N. C.; Sudhakar, K.; Tahir, M. Metal-organic framework-based photocatalysts for carbon dioxide reduction to methanol: A review on progress and application. *J. CO2 Util.* **2021**, *43*, No. 101374.

(5) Francke, R.; Schille, B.; Roemelt, M. Homogeneously Catalyzed Electroreduction of Carbon Dioxide - Methods, Mechanisms, and Catalysts. *Chem. Rev.* **2018**, *118* (9), 4631−4701.

(6) Liang, Z.; Wang, H. Y.; Zheng, H.; Zhang, W.; Cao, R. Porphyrin-Based Frameworks for Oxygen Electrocatalysis and Catalytic Reduction of Carbon Dioxide. *Chem. Soc. Rev.* **2021**, *50* (4), 2540−2581.

(7) Nielsen, D. U.; Hu, X. M.; Daasbjerg, K.; Skrydstrup, T. Chemically and Electrochemically Catalysed Conversion of CO2 to CO with Follow-up Utilization to Value-Added Chemicals. *Nat. Catal.* **2018**, *1* (4), 244−254.

(8) Wang, S.; Feng, K.; Zhang, D.; Yang, D.; Xiao, M.; Zhang, C.; He, L.; Yan, B.; Ozin, G. A.; Sun, W. Stable Cu Catalysts Supported by Two-Dimensional SiO2 with Strong Metal−Support Interaction. *Adv. Sci.* **2022**, *9* (9), No. 2104972.

(9) Creissen, C. E.; Fontecave, M. Keeping Sight of Copper in Single-Atom Catalysts for Electrochemical Carbon Dioxide Reduction. *Nat. Commun.* **2022**, *13* (1), 1−4.

(10) Have, I. C. Te; Kromwijk, J. J. G.; Monai, M.; Ferri, D.; Sterk, E. B.; Meirer, F.; Weckhuysen, B. M. Uncovering the Reaction Mechanism behind CoO as Active Phase for CO2 Hydrogenation. *Nat. Commun.* **2022**, *13* (1), 1−11.

(11) Ulmer, U.; Dingle, T.; Duchesne, P. N.; Morris, R. H.; Tavasoli, A.; Wood, T.; Ozin, G. A. Fundamentals and Applications of Photocatalytic CO2Methanation. *Nat. Commun.* **2019**, *10* (1), 1−12.

(12) Dry, M. E. The Fischer−Tropsch Process: 1950−2000. *Catal. Today* **2002**, *71* (3−4), 227−241.

(13) Juneau, M.; Vonglis, M.; Hartvigsen, J.; Frost, L.; Bayerl, D.; Dixit, M.; Mpourmpakis, G.; Morse, J. R.; Baldwin, J. W.; Willauer, H. D.; Porosoff, M. D. Assessing the Viability of K-Mo2C for Reverse Water−Gas Shift Scale-up: Molecular to Laboratory to Pilot Scale. *Energy Environ. Sci.* **2020**, *13* (8), 2524−2539.

(14) Yu, Y. X.; Yang, J.; Zhu, K. K.; Sui, Z. J.; Chen, D.; Zhu, Y. A.; Zhou, X. G. High-Throughput Screening of Alloy Catalysts for Dry Methane Reforming. *ACS Catal.* **2021**, *11* (14), 8881−8894.

(15) Cheng, Q.; Yao, X.; Ou, L.; Hu, Z.; Zheng, L.; Li, G.; Morlanes, N.; Cerrillo, J. L.; Castaño, P.; Li, X.; Gascon, J.; Han, Y. Highly Efficient and Stable Methane Dry Reforming Enabled by a Single-Site Cationic Ni Catalyst. *J. Am. Chem. Soc.* **2023**, *145* (46), 25109−25119.

(16) Mette, K.; Kühl, S.; Düdder, H.; Kähler, K.; Tarasov, A.; Muhler, M.; Behrens, M. Stable Performance of Ni Catalysts in the Dry Reforming of Methane at High Temperatures for the Efficient Conversion of CO2 into Syngas. *ChemCatChem.* **2014**, *6* (1), 100−104.

(17) Lercher, J. A.; Bitter, J. H.; Hally, W.; Niessen, W.; Seshan, K. Design of Stable Catalysts for Methane-Carbon Dioxide Reforming. *Stud. Surf. Sci. Catal.* **1996**, *101*, 463−472.

(18) Tang, S.; Ji, L.; Lin, J.; Zeng, H. C.; Tan, K. L.; Li, K. CO2 Reforming of Methane to Synthesis Gas over Sol−Gel-Made Ni/γ-Al2O3 Catalysts from Organometallic Precursors. *J. Catal.* **2000**, *194* (2), 424−430.

(19) Bian, Z.; Das, S.; Wai, M. H.; Hongmanorom, P.; Kawi, S. A Review on Bimetallic Nickel-Based Catalysts for CO2 Reforming of Methane. *ChemPhysChem* **2017**, *18* (22), 3117−3134.

(20) Guharoy, U.; Reina, T. R.; Liu, J.; Sun, Q.; Gu, S.; Cai, Q. A Theoretical Overview on the Prevention of Coking in Dry Reforming of Methane Using Non-Precious Transition Metal Catalysts. *J. CO2 Util.* **2021**, *53*, No. 101728.

(21) Ighalo, J. O.; Amama, P. B. Recent Progress in the Design of Dry Reforming Catalysts Supported on Low-Dimensional Materials. *J. CO2 Util.* **2024**, *81*, No. 102734.

(22) Vogt, C.; Kranenborg, J.; Monai, M.; Weckhuysen, B. M. Structure Sensitivity in Steam and Dry Methane Reforming over Nickel: Activity and Carbon Formation. *ACS Catal.* **2020**, *10* (2), 1428−1438.

(23) Wittich, K.; Krämer, M.; Bottke, N.; Schunk, S. A. Catalytic Dry Reforming of Methane: Insights from Model Systems. *ChemCatChem.* **2020**, *12* (8), 2130−2147.

(24) Pizzolitto, C.; Pupulin, E.; Menegazzo, F.; Ghedini, E.; Di Michele, A.; Mattarelli, M.; Cruciani, G.; Signoretto, M. Nickel Based Catalysts for Methane Dry Reforming: Effect of Supports on Catalytic Activity and Stability. *Int. J. Hydrogen Energy* **2019**, *44* (52), 28065−28076.

(25) Zhu, Q.; Liu, Y.; Qin, X.; Liu, L.; Ren, Z.; Tao, X.; Wang, C.; Wang, H.; Li, L.; Liu, X.; Chen, L.; Wang, L.; Xiao, F.-S. Zeolite Fixed Cobalt−Nickel Nanoparticles for Coking and Sintering Resistance in Dry Reforming of Methane. *Chem. Eng. Sci.* **2023**, *280*, No. 119030.

(26) Sasson Bitters, J.; He, T.; Nestler, E.; Senanayake, S. D.; Chen, J. G.; Zhang, C. Utilizing Bimetallic Catalysts to Mitigate Coke Formation in Dry Reforming of Methane. *J. Energy Chem.* **2022**, *68*, 124−142.

(27) Arora, S.; Prasad, R. An Overview on Dry Reforming of Methane: Strategies to Reduce Carbonaceous Deactivation of Catalysts. *RSC Adv.* **2016**, *6* (110), 108668−108688.

(28) Buelens, L. C.; Galvita, V. V.; Poelman, H.; Detavernier, C.; Marin, G. B. Super-Dry Reforming of Methane Intensifies CO2 Utilization via Le Chatelier's Principle. *Science* **2016**, *354* (6311), 449−452.

(29) Abdullah, B.; Abd Ghani, N. A.; Vo, D. V. N. Recent Advances in Dry Reforming of Methane over Ni-Based Catalysts. *J. Clean. Prod.* **2017**, *162*, 170−185.

https://doi.org/10.1021/acsomega.4c09539
ACS Omega 2025, 10, 16102−16113

(30) Zhang, Z.; Zhang, Y.; Liu, L. Role and Mechanism of Calcium-Based Catalysts for Methane Dry Reforming: A Review. *Fuel* **2024**, *355*, No. 129329.
(31) ZHANG, R.; XIA, G.; LI, M.; WU, Y.; NIE, H.; LI, D. Effect of Support on the Performance of Ni-Based Catalyst in Methane Dry Reforming. *J. Fuel Chem. Technol.* **2015**, *43* (11), 1359−1365.
(32) Shah, M.; Al Mesfer, M. K.; Danish, M. Design and Optimization of Ni−Fe−La Based Catalytic System for CO2 Utilization for Sustainable Syngas Production via Dry Reforming of Methane. *J. Energy Inst.* **2023**, *110*, No. 101346.
(33) Aramouni, N. A. K.; Touma, J. G.; Tarboush, B. A.; Zeaiter, J.; Ahmad, M. N. Catalyst Design for Dry Reforming of Methane: Analysis Review. *Renew. Sustain. Energy Rev.* **2018**, *82*, 2570−2585.
(34) Zhang, Q.; Gao, S.; Yu, J. Metal Sites in Zeolites: Synthesis, Characterization, and Catalysis. *Chem. Rev.* **2022**, *123*, 6039.
(35) Jing, W.; Shen, H.; Qin, R.; Wu, Q.; Liu, K.; Zheng, N. Surface and Interface Coordination Chemistry Learned from Model Heterogeneous Metal Nanocatalysts: From Atomically Dispersed Catalysts to Atomically Precise Clusters. *Chem. Rev.* **2022**, *123*, 5948.
(36) Hamisu, A. M.; Ariffin, A.; Wibowo, A. C. Cation Exchange in Metal-Organic Frameworks (MOFs): The Hard-Soft Acid-Base (HSAB) Principle Appraisal. *Inorg. Chim. Acta* **2020**, *511*, No. 119801.
(37) Pearson, R. G. Hard and Soft Acids and Bases. *J. Am. Chem. Soc.* **1963**, *85* (22), 3533−3539.
(38) Devos, J.; Sushkevich, V. L.; Khalil, I.; Robijns, S.; de Oliveira-Silva, R.; Sakellariou, D.; van Bokhoven, J.; Dusselier, M. Enhancing the Acidity Window of Zeolites by Low-Temperature Template Oxidation with Ozone. *J. Am. Chem. Soc.* **2024**, *146*, 27047.
(39) Akri, M.; Zhao, S.; Li, X.; Zang, K.; Lee, A. F.; Isaacs, M. A.; Xi, W.; Gangarajula, Y.; Luo, J.; Ren, Y.; Cui, Y. T.; Li, L.; Su, Y.; Pan, X.; Wen, W.; Pan, Y.; Wilson, K.; Li, L.; Qiao, B.; Ishii, H.; Liao, Y. F.; Wang, A.; Wang, X.; Zhang, T. Atomically Dispersed Nickel as Coke-Resistant Active Sites for Methane Dry Reforming. *Nat. Commun.* **2019**, *10* (1), 1−10.
(40) Mette, K.; Kühl, S.; Tarasov, A.; Willinger, M. G.; Kröhnert, J.; Wrabetz, S.; Trunschke, A.; Scherzer, M.; Girgsdies, F.; Düdder, H.; Kähler, K.; Ortega, K. F.; Muhler, M.; Schlögl, R.; Behrens, M.; Lunkenbein, T. High-Temperature Stable Ni Nanoparticles for the Dry Reforming of Methane. *ACS Catal.* **2016**, *6* (10), 7238−7248.
(41) Gregg, S. J.; Sing, K. S. W. *Adsorption, Surface Area and Porosity*; 2nd Ed., Academic Press: 1982.
(42) Chen, B. H.; Chao, Z. S.; He, H.; Huang, C.; Liu, Y. J.; Yi, W. J.; Wei, X. L.; An, J. F. Towards a Full Understanding of the Nature of Ni(II) Species and Hydroxyl Groups over Highly Siliceous HZSM-5 Zeolite Supported Nickel Catalysts Prepared by a Deposition−Precipitation Method. *Dalt. Trans.* **2016**, *45* (6), 2720−2739.
(43) Barton, R. R.; Carrier, M.; Segura, C.; Fierro, J. L. G.; Escalona, N.; Peretti, S. W. Ni/HZSM-5 Catalyst Preparation by Deposition-Precipitation. Part 1. Effect of Nickel Loading and Preparation Conditions on Catalyst Properties. *Appl. Catal. A Gen.* **2017**, *540*, 7−20.
(44) Holder, C. F.; Schaak, R. E. Tutorial on Powder X-Ray Diffraction for Characterizing Nanoscale Materials. *ACS Nano* **2019**, *13* (7), 7359−7365.
(45) Huang, Q.; Wang, J.; Sun, Y.; Li, X.; Wang, X.; Zhao, Z. Gas-Sensing Properties of Composites of Y-Zeolite and SnO2. *J. Mater. Sci.* **2018**, *53* (9), 6729−6740.
(46) Du, L.; Ginting, E.; Zhou, J. Morphology and Chemical States of Ni Supported on Ti-Modified CeOx(111) Interfaces. *Surf. Sci.* **2020**, *699*, No. 121624.
(47) Islam, M. B.; Yanagida, M.; Shirai, Y.; Nabetani, Y.; Miyano, K. NiOx Hole Transport Layer for Perovskite Solar Cells with Improved Stability and Reproducibility. *ACS Omega* **2017**, *2* (5), 2291−2299.
(48) Zhan, Y.; Song, K.; Shi, Z.; Wan, C.; Pan, J.; Li, D.; Au, C.; Jiang, L. Influence of Reduction Temperature on Ni Particle Size and Catalytic Performance of Ni/Mg(Al)O Catalyst for CO2 Reforming of CH4. *Int. J. Hydrogen Energy* **2020**, *45* (4), 2794−2807.
(49) Adhikari, D.; Whitcomb, C. A.; Zhang, W.; Zhang, S.; Davis, R. J. Revisiting the Influence of Ni Particle Size on the Hydrogenation of CO2 to CH4 over Ni/CeO2. *J. Catal.* **2024**, *438*, No. 115708.
(50) Ross, J. R. H.; Steel, M. C. F. Mechanism of the Steam Reforming of Methane over a Coprecipitated Nickel-Alumina Catalyst. *J. Chem. Soc. Faraday Trans. 1 Phys. Chem. Condens. Phases* **1973**, *69* (0), 10−21.
(51) Schulz-Ekloff, G.; Czarnetzki, L.; Zukal, A. Non-Isothermal Reduction Kinetics and Reducibilities of Nickel and Cobalt Faujasites. *J. Chem. Soc. Faraday Trans. 1 Phys. Chem. Condens. Phases* **1987**, *83* (9), 3015−3025.
(52) Gac, W.; Greluk, M.; Słowik, G.; Millot, Y.; Valentin, L.; Dzwigaj, S. Effects of Dealumination on the Performance of Ni-Containing BEA Catalysts in Bioethanol Steam Reforming. *Appl. Catal. B Environ.* **2018**, *237*, 94−109.
(53) Hulea, V.; Fajula, F. Ni-Exchanged AlMCM-41-An Efficient Bifunctional Catalyst for Ethylene Oligomerization. *J. Catal.* **2004**, *225*, 213−222.
(54) Mosqueda-Jiménez, B. I.; Jentys, A.; Seshan, K.; Lercher, J. A. Reduction of Nitric Oxide by Propene and Propane on Ni-Exchanged Mordenite. *Appl. Catal. B Environ.* **2003**, *43* (2), 105−115.
(55) Lin, T. J.; Meng, X.; Shi, L. Ni-Exchanged Y-Zeolite: An Efficient Heterogeneous Catalyst for Acetylene Hydrocarboxylation. *Appl. Catal. A Gen.* **2014**, *485*, 163−171.
(56) Verhaak, M. J. F. M.; van Dillen, A. J.; Geus, J. W. Measuring the Acid-Base Properties of Supported Nickel Catalysts Using Temperature-Programmed Desorption of Ammonia. *Appl. Catal. A Gen.* **1993**, *105* (2), 251−269.
(57) González-Castaño, M.; Dorneanu, B.; Arellano-García, H. The Reverse Water Gas Shift Reaction: A Process Systems Engineering Perspective. *React. Chem. Eng.* **2021**, *6* (6), 954−976.
(58) Wei, L.; Haije, W.; Kumar, N.; Peltonen, J.; Peurla, M.; Grenman, H.; De Jong, W. Influence of Nickel Precursors on the Properties and Performance of Ni Impregnated Zeolite 5A and 13X Catalysts in CO2Methanation. *Catal. Today* **2021**, *362*, 35−46.
(59) Kim, J.; Han, S. W.; Kim, J. C.; Ryoo, R. Supporting Nickel to Replace Platinum on Zeolite Nanosponges for Catalytic Hydroisomerization of n -Dodecane. *ACS Catal.* **2018**, *8* (11), 10545−10554.
(60) Seo, S. M.; Moon, D. J.; An, J.; Jeong, H. K.; Lim, W. T. Time-Dependent Ni2+-Ion Exchange in Zeolites y (FAU, Si/Al = 1.56) and Their Single-Crystal Structures. *J. Phys. Chem. C* **2016**, *120* (50), 28563−28574.
(61) Song, M.; Eom, E.; Shin, J. W.; Cho, H. S.; Kim, J. C.; Jo, C. Mercaptoamine-Assisted Post-Encapsulation of Metal Nanoparticles within Preformed Zeolites and Their Analogues for Hydroisomerization and Methane Decomposition. *Angew. Chemie Int. Ed.* **2023**, *62*, No. e202303503.
(62) Safidine, Z.; Ghebache, Z.; Lamouri, S. Thermoelectrical Characterization of New Material Based on PANI/Zeolite HY Composite, Used for the Detection of Carbon Dioxide. *Polym. J.* **2013**, *45* (9), 946−954.
(63) O'Brien, J.; Curtin, T.; O'Dwyer, T. F. An Investigation into the Adsorption of Aniline from Aqueous Solution Using H-Beta Zeolites and Copper-Exchanged Beta Zeolites. *Adsorpt. Sci. Technol.* **2005**, *23*, 255−266.
(64) Hamisu, A. M.; Wardana, F. Y.; Ariffin, A.; Baig, I.; Malliakas, C. D.; Wibowo, A. C. A New Synthetic Approach for Substitutional Solid Solutions in a 3D Coordination Polymer: Cation Vacancy, and Tunable Photoluminescence. *J. Solid State Chem.* **2019**, *279*, No. 120948.
(65) Wang, S.; Cao, J.; Jia, W.; Guo, W.; Yan, S.; Wang, Y.; Zhang, P.; Chen, H. Y.; Huang, S. Single Molecule Observation of Hard−Soft-Acid−Base (HSAB) Interaction in Engineered Mycobacterium Smegmatis Porin A (MspA) Nanopores. *Chem. Sci.* **2020**, *11* (3), 879−887.

https://doi.org/10.1021/acsomega.4c09539
ACS Omega 2025, 10, 16102−16113